remote sensing

Article

Rainfall Erosivity Characteristics during 1961–2100 in the Loess Plateau, China

Xiuping Li [1,2], Peiqing Xiao [2,*], Shilong Hao [1] and Zhihui Wang [2]

[1] College of Surveying and Geo-Informatics, North China University of Water Resources and Electric Power, Zhengzhou 450046, China; z20211151038@stu.ncwu.edu.cn (X.L.); haoshilong@ncwu.edu.cn (S.H.)
[2] Key Laboratory of Soil and Water Conservation on the Loess Plateau of Ministry of Water Resources, Yellow River Institute of Hydraulic Research, Zhengzhou 450003, China; hezimiao@ncwu.edu.cn
* Correspondence: 201501114@stu.ncwu.edu.cn; Tel.: +86-136-6385-8913

Abstract: Rainfall erosivity, which signifies the inherent susceptibility of soil erosion induced by precipitation, plays a fundamental role in formulating a comprehensive soil loss equation (RUSLE). It stands as a crucial determinant among the foundational factors considered in a comprehensive soil loss equation's establishment. Nonetheless, the prediction and quantification of future alterations in rainfall erosivity under the influence of global warming have been relatively limited. In this study, climate change was widely evaluated and 10 preferred global climate models in the Loess Plateau were selected by using the data sets of 27 models simulating climate change and the CN05.1 data set provided by the latest CMIP6. The monthly precipitation forecast data were obtained by using the delta downscaling method. Combined with trend analysis, significance test, and coefficient of variation, the annual rainfall erosivity during 1961–2100 under four SSP scenarios was analyzed and predicted. Among the 27 GCM models used in this paper, the most suitable climate models for simulating monthly precipitation in the Loess Plateau were CMCC-CM2-SR5, CMCC-ESM2, TaiESM1, EC-Earth3, EC-Earth-Veg-LR, INM-CM4-8, CAS-ESM2-0, EC-Earth-Veg, ACCESS-ESM1-5, and IPSL-CM6A-LR. In comparison to the base period (1961–1990), during the historical period (1961–2014), the average annual rainfall erosivity on the Loess Plateau amounted to 1259.64 $MJ \cdot mm \cdot hm^{-2} \cdot h^{-1} \cdot a^{-1}$, showing an insignificant downward trend. In the northwest of Ningxia, Yulin City and Yanan City showed a significant upward trend. In the future period (2015–2100), the annual rainfall erosivity continues to constantly change and increase. The potential average increase in rainfall erosivity is about 13.48–25.86%. In terms of spatial distribution, most areas showed an increasing trend. Among these regions, the majority of encompassed areas within Shanxi Province, central Shaanxi, and Inner Mongolia increased greatly, which was not conducive to soil and water conservation and ecological environment construction. This study offers a scientific reference for the projected future erosivity characteristics of the Loess Plateau.

Keywords: global climate model; annual rainfall erosivity; Loess Plateau; emission scenarios; future change projections

check for updates

Citation: Li, X.; Xiao, P.; Hao, S.; Wang, Z. Rainfall Erosivity Characteristics during 1961–2100 in the Loess Plateau, China. *Remote Sens.* **2024**, *16*, 661. https://doi.org/10.3390/rs16040661

Academic Editors: Baojie He, Siliang Yang, K. Venkatachalam, Amos Darko, Gad Levy and Balázs Székely

Received: 13 October 2023
Revised: 30 January 2024
Accepted: 6 February 2024
Published: 12 February 2024

1. Introduction

Despite nearly a century of research and promotion efforts, soil erosion due to water, wind, and tillage still threatens ecological security and sustainable development in many areas around the world [1,2]. Climate change is considered the primary natural cause of soil erosion [3]. The spatiotemporal variation in rainfall–runoff erosivity caused by climate change has great significant implications for regional soil erosion [4,5].

However, human activities are altering the global climate in unprecedented and potentially irreversible ways [6]. Extreme weather events in Europe caused by cold air masses and heat domes leading to heat waves in North America are once again demonstrating that global climate change is reshaping Earth's temperature patterns [7,8]. As human activities continue to emit greenhouse gases into the atmosphere, there is also a growing accumulation of excess energy within the climate system. This energy is eventually released through extreme weather events, and extreme droughts and heavy rainfall events will become more frequent as greenhouse gas emissions increase [9,10].

Predicting global soil erosion changes from the perspective of future climate change scenarios is of great significance for assessing the ecological risks caused by climate change [11], but it still requires collaborative evaluation of regional and local information. Due to the combined impact of climate, topography, vegetation, soil, and human interventions, the Loess Plateau has a wide area of soil erosion and has become one of the most severe regions of soil erosion in China [12,13]. Rainfall erosivity indicates the potential capacity of rainfall to cause soil erosion [14]. It constitutes the primary driving force behind soil water erosion and stands as one of the key factors of modeling soil erosion and water environment dynamics. Changes in precipitation patterns caused by climate change will significantly affect future rainfall erosivity. Several existing studies have predicted future changes in rainfall erosivity in the United States [11], Turkey [15], Europe [16], Australia [17], China [18], and India [19]. Most of these studies believe that future rainfall erosivity will increase significantly at the regional scale. It is necessary to determine the changes in rainfall erosivity in various regions of the Loess Plateau, so as to lay a foundation for further discussions on the influence and contribution of rainfall erosivity to sediment yield and sediment transport.

A new phase of the international Coupled Model Intercomparison Project (Phase 6) has been initiated by the World Climate Research Programme (WCRP) to address emerging scientific inquiries within the realm of climate change. One of the central themes in earlier reports by the Intergovernmental Panel on Climate Change (IPCC) has been climate predictions under various scenarios. These findings can illustrate the climate consequences and socioeconomic hazards associated with various policy choices, thereby serving as a vital scientific foundation for governmental decision-making. Leveraging different shared socioeconomic pathways (SSPs) and the most recent anthropogenic emission trends, CMIP6 introduced a fresh scenario known as the Scenario Model Intercomparison Project (ScenarioMIP) [20]. The ScenarioMIP projection scenario is a composite representation formed by combining various SSPs and radiative forcing. An SSP describes the possible development of future societies with the impact of climate change or influence of climate. According to the relative priority of the experiment, the ScenarioMIP experiment is divided into two levels. As the core experiment, Tier-1 includes four paths, SSP1, SSP2, SSP3, and SSP5, which represent the four paths of sustainable development, moderate development, local development, and conventional development. Compared with the CMIP5(RCP) scenario experiment, ScenarioMIP produces changes in land use and emission pathways that correspond to a range of potential future socioeconomic development scenarios. It places a strong emphasis on maintaining consistency between future radiative forcing scenarios and shared socioeconomic scenarios, and its improvement of the climatological mean state simulation of rainfall is particularly obvious [21].

Due to rapid advancements in atmospheric detection and computer technology, the spatial resolution of GCM models has reached several tens of kilometers, which can predict and analyze the climate situation at the global scale. However, their output resolutions are still low and lack regional information; their regional climate change simulations and predictions for future climate change are characterized by a low level of accuracy. For this reason, the downscaling method is usually used to transform the large-scale data to attain regional climate predictions; the aim is to transform the low-resolution data offered by global climate models into high-resolution data at the regional level. Downscaling methods are mainly divided into statistical downscaling and dynamic downscaling. In contrast to statistical downscaling, dynamic downscaling necessitates a substantial amount of computational resources, and is affected by many factors. There are errors and uncertainties, and it cannot truly reflect climate change on the geographical scale [22]. The delta downscaling method uses low-spatial-resolution monthly climate data and high-spatial-resolution reference climate data as input data. Different from direct interpolation, this method can introduce the influence of topography on climate [23], and can obtain accurate downscaling climate data on small geographic scales. Therefore, more people choose the delta downscaling method to improve the accuracy of climate model data [24,25].

At present, there are few studies on the application of SSP scenarios to predict the future rainfall erosivity in the Loess Plateau. Because of the wide range in the Loess Plateau, building upon existing research, it is imperative to conduct further assessments of rainfall erosivity changes throughout the 21st century. Therefore, this paper evaluates the predictive ability of 27 climate model rainfall data sets provided by CMIP6 in the historical period (1961–2014), and selects 10 climate models with strong simulation ability to predict the future period (2015–2100). Interannual changes and spatial trends of rainfall erosivity under the SSP scenarios (SSP1-2.6, SSP2-4.5, SSP3-7.0, and SSP5-8.5) on the Loess Plateau are analyzed. This study will furnish a scientific underpinning of future rainfall erosivity prediction. It also provides a reference for soil erosion control, soil and water conservation, and ecological environment protection in the Loess Plateau.

2. Materials and Methods

2.1. Study Area

The Loess Plateau, which is the largest loess accumulation area in the world, covers approximately 640,000 square kilometers. The Loess Plateau (Figure 1) has continental climate characteristics. The study area primarily consists of plateau terrain, with higher elevations in the northwest and lower elevations in the southeast. The loess is generally dominated by silt particles, the soil is loose, the surface material is unstable, and erosion and collapse can easily occur in the event of external forces. Since the 1970s, extensive soil and water conservation measures have been put into effect. Especially since 1999, the project of returning farmland to forest (grass) has been implemented, which has effectively alleviated soil erosion. Future increases in extreme rainfall events will bring challenges to the existing soil and water conservation measures.

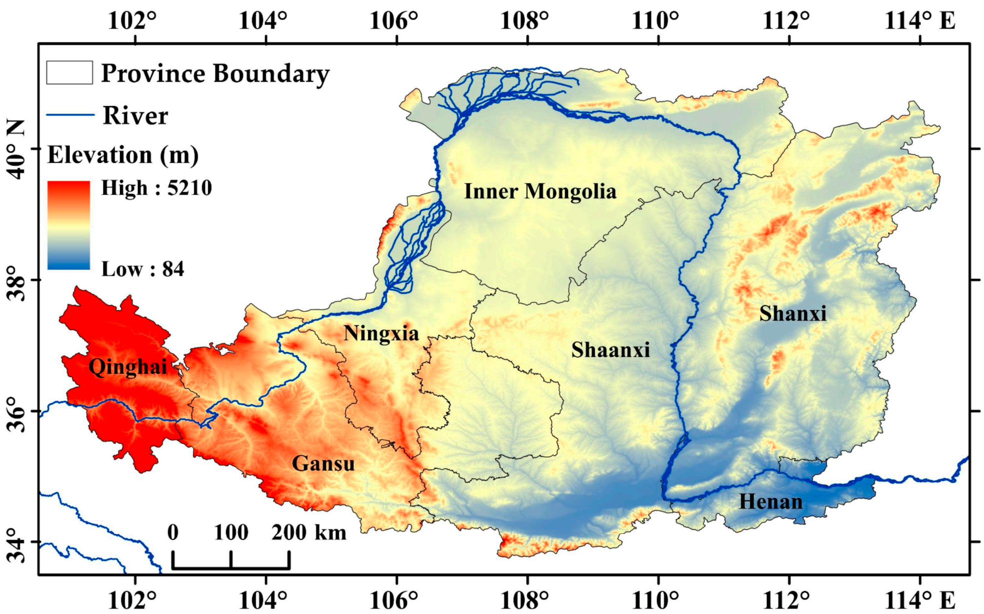

Figure 1. Geographical location of the Loess Plateau.

2.2. Data

The data required for the delta downscaling method include a long-term series of low-resolution climate data sets and high-resolution reference climate data sets. The former uses the simulated rainfall data set provided by CMIP6 participating in the Tier-1 experiment. The Tier-1 experiment is the core experiment in ScenarioMIP, and most of the modes participate in this experiment [26]. Therefore, the four scenarios of SSP1-2.6, SSP2-4.5, SSP3-7.0, and SSP5-8.5 in the Tier-1 experiment were selected in this paper, and detailed information is shown in Table 1. Taking into account the integrity of the data, this paper screens out the monthly historical data (1961–2014) under 27 kinds of r1ilpi operations and the forecast data (2015–2100) under the above four scenarios (Table 2). The latter data sets use the CN05.1 precipitation data set [27]. The time span was 1961–2018, and the spatial resolution was 25 km. The data set was derived from precipitation observation data collected at 2416 meteorological stations across China, resulting in a gridded data set. The interpolation method of "anomaly approach" was used to reflect the precipitation situation in China more accurately. Its applications encompass a broad spectrum, including its utilization in climate model simulation evaluation and the analysis of contemporary climate change. In the data accuracy verification stage, we used the ERA5 reanalysis data from the European Centre for Medium-Range Weather Forecasts (ECMWF) with a spatial resolution of 0.25°, which can more objectively verify the accuracy of the downscaled data.

Table 1. ScenarioMIP experiment designs (SSP means shared socioeconomic pathways).

Test Level	Scenario Name	Forcing Category	2100 Forcing ($W{\cdot}m^{-2}$)	SSP
Tier-1	SSP1-2.6	Low	2.6	1
	SSP2-4.5	Medium	4.5	2
	SSP3-7.0	High	7.0	3
	SSP5-8.5	High	8.5	5

Table 2. Basic information on global climate models used in this study and their references.

NO	Model	Institution and References
1	ACCESS-CM2	Commonwealth Scientific and Industrial Research Organization, Australia [28]
2	ACCESS-ESM1-5	Commonwealth Scientific and Industrial Research Organization, Australia [29]
3	AWI-CM-1-1-MR	Alfred Wegener Institute, Helmholtz Centre for Polar and Marine Research, Germany [30]
4	BCC-CSM2-MR	Beijing Climate Center, China [31]
5	CAMS-CSM1-0	Chinese Academy of Meteorological Sciences, China [32]
6	CanESM5	Canadian Centre for Climate Modelling and Analysis,Canada [33]
7	CanESM5-1	Canadian Centre for Climate Modelling and Analysis, Canada [34]
8	CAS-ESM2-0	Chinese Academy of Sciences, China [35]
9	CESM2-WACCM	National Center for Atmospheric Research, USA [36]
10	CMCC-CM2-SR5	Fondazione Centro Euro-Mediterraneo sui Cambiamenti Climatici, Italy [37]
11	CMCC-ESM2	Centro Euro-Mediterraneo sui Cambiamenti Climatici, Italy [38]
12	EC-Earth3	EC-Earth consortium, Europe [39]
13	EC-Earth3-Veg	EC-Earth consortium, Europe [40]
14	EC-Earth-Veg-LR	EC-Earth consortium, Europe [40]
15	FGOALS-f3-L	Chinese Academy of Sciences, China [41]
16	FGOALS-g3	Chinese Academy of Sciences, China [42]
17	IITM-ESM	Indian Institute of Tropical Meteorology, India [43]
18	INM-CM4-8	Institute for Numerical Mathematics, Russia [44]
19	INM-CM5-0	Institute for Numerical Mathematics, Russia [45]
20	IPSL-CM6A-LR	Institut Pierre Simon Laplace, France [46]
21	KACE-1-0-G	National Institute of Meteorological Sciences-Korea Met. Administration, Korea [47]
22	MIROC6	Japan Agency for Marine–Earth Science and Technology, Japan [48]
23	MPI-ESM1-2-HR	Max Planck Institute for Meteorology, Germany [49]
24	MPI-ESM1-2-LR	Max Planck Institute for Meteorology, Germany [50]
25	MRI-ESM2-0	Meteorological Research Institute, Japan [51]
26	NorESM2-LM	Norwegian Climate Centre, Norway [52]
27	TaiESM1	Norwegian Climate Centre, Norway [53]

In order to perform a more detailed assessment of rainfall's spatial variation, the above CMIP6, CN05.1, and ERA5 precipitation data sets were resampled to a 500 m resolution using bilinear interpolation.

2.3. Methods

2.3.1. Statistical Downscaling

Due to the prediction model's low spatial resolution and lack of consistency, it is usually necessary to use downscaling technology to transform the large-scale and low-resolution model information into small-scale and high-resolution regional precipitation change information, so as to obtain a relatively accurate regional climate scenario. The delta downscaling method is a future climate scenario generation method recommended by the National Evaluation Center of the United States. It is also a commonly used downscaling method with good results. Liu et al. [54] compared the adaptability of three downscaling methods, including the delta downscaling method, in the Hanjiang River, and found that the data processed by the delta downscaling method performed well in responding to extreme precipitation indicators. Navano et al. [55] created a collection of bioclimatic index data using the delta downscaling method to evaluate the influence of climate change on biodiversity. Using the delta downscaling method, Peng et al. [56] assessed the temporal and spatial variations in potential evapotranspiration from 2011 to 2100. They conducted this analysis with data corresponding to four distinct concentration pathways under the RCP scenario. The delta downscaling method superimposes the variation characteristics of the simulated grid climate elements on the sequence of climate elements measured in the base period to reconstruct the scenarios of climate elements. For the precipitation scenario, the delta downscaling method was used to compare the precipitation in different periods of each simulation grid with the simulated average precipitation in the base period, calculate the absolute change rate of precipitation in each period of each simulation grid, and then multiply the measured average precipitation in each base period with the change rate of the grid to obtain the precipitation scenarios in different periods on the reconstructed grid. The calculation method is as follows:

$$P_f = P_0 \frac{P_{C_f}}{P_{C_0}} \quad (1)$$

Among them, P_f is the grid rainfall data reconstructed by the delta downscaling method; P_{C_f} is the simulated grid precipitation data of a certain period; P_{C_0} is the simulated grid multi-year average precipitation data of the base period; and P_0 is the measured multi-year average precipitation data of the base period. It can be considered that the change rate of simulated grid precipitation is:

$$Delta(P) = \frac{P_{C_f}}{P_{C_0}} \quad (2)$$

Incorporated into this methodology are considerations for the influences of topography and land cover characteristics, resulting in more reliable and detailed meteorological information. Therefore, the delta downscaling method was adopted for spatial downscaling to acquire a high-resolution climate data set for the prediction period in the Loess Plateau.

2.3.2. Multi-Model Ensemble (MME)

In previous studies, some scholars mostly used the output of a single GCM model as experimental data. It does not accurately predict future climate change [57]. A multi-model ensemble can reduce the uncertainty of multi-model simulation and restore real data. Existing research has confirmed that the results of multi-model ensembles are better than those of single models [58]. In this study, out of the 27 models available, 10 models demonstrating superior simulation capabilities were chosen, and the future climate prediction data of the Loess Plateau were obtained by a multi-model ensemble method. The calculation method is as follows:

$$SM = \frac{1}{n}\sum_{i=1}^{n} GCM_i \quad (3)$$

Among them, SM refers to the simulation data after the multi-model set; and n refers to the GCM model data with good simulation ability screened according to the MAE. In this paper, n = 10.

2.3.3. Evaluation of the Multi-Model Adaptability

In the prediction and evaluation of continuous values, coefficient of determination (R^2), Root Mean Square Error (RMSE), and Mean Absolute Error (MAE) are the most commonly used evaluation indicators. RMSE provides insight into the extent of dispersion within a data set, and a lower RMSE indicates that the model has a more accurate prediction. R^2 represents the coefficient of determination, serving as an indicator of the proportion of the overall variability in the dependent variable that can be accounted for by the independent variable through the regression relationship. MAE is defined as the average of the absolute errors between the observed and predicted values. Similar to deviation, but because the deviation is absolute, there will be no positive and negative offset. This enables a more accurate depiction of the error in the simulated values, portraying better with the real circumstances. Therefore, this paper uses R^2, RMSE, and MAE indicators to quantify the model simulation performance. The calculation method is as follows:

$$RMSE = \sqrt{\frac{\sum_{i=1}^{N}(O_i - P_i)^2}{N}} \tag{4}$$

$$R^2 = \frac{\left[\sum_{i=1}^{N}\left(O_i - \overline{O}\right)\left(P_i - \overline{P}\right)\right]^2}{\sum_{i=1}^{N}\left(O_i - \overline{O}\right)^2\sum_{i=1}^{N}\left(P_i - \overline{P}\right)^2} \tag{5}$$

$$MAE = \frac{1}{N}\sum_{i=1}^{N}|P_i - O_i| \tag{6}$$

P_i represents the data processed by the delta downscaling method, O_i represents the observed data, and N is the number of samples.

The comprehensive score is based on the above indicators according to the rank scoring method proposed by Chen et al. [59]. The simulation performance index R_j of a single model j can be obtained by sorting the models, which is defined as follows:

$$R_j = \frac{\sum_{j=1}^{N} S_j}{S_j} \tag{7}$$

Among them, S_j is the ranking of pattern j, which is obtained by summing the corresponding rankings of the above three indicators; and N denotes the total number of patterns (N = 27). According to the normalization principle, R_j is converted into a percentile score for comprehensive evaluation, named W_j. The higher the W_j, the better the simulation performance of the model.

2.3.4. Rainfall Erosivity Calculations

In this paper, the method proposed by Zhang et al. [60] is used to calculate the rainfall erosivity in the Loess Plateau. The calculation method is as follows:

$$R = \alpha_4 F^{\beta_4} \tag{8}$$

$$F = 1 \cdot N^{-1}\sum_{i=1}^{N}\left[\left(\sum_{j=1}^{12} {P_{i,j}}^2\right) \cdot \left(\sum_{j=1}^{12} P_{i,j}\right)^{-1}\right] \tag{9}$$

In the formula, $P_{i,j}$ is the rainfall (mm) in the jth month of the i year, N is the number of years, R is the multi-year average rainfall erosivity in MJ·mm·hm^{-2}·h^{-1}, and α_4 and β_4 are the model parameters.

In particular, the model for calculating rainfall erosivity proposed by Zhang et al. is a nonlinear structure, so the model parameters are determined through the utilization of the nonlinear regression analysis method. The model parameters correspond to the monthly rainfall parameters calculated by Zhang et al., namely, α_4 = 0.1833 and β_4 = 1.9957.

2.3.5. Change Trend and Significance Test

Tests for detecting significant trends in climate time series can be divided into parametric or non-parametric tests. Non-parametric testing does not necessitate adherence to a specific distribution within the sample and remains unaffected even when there are a few outliers. Therefore, this paper uses two non-parametric test methods, the Sen's Slope and Mann–Kendall (M-K) tests, to detect the grid simulation R data from 1961 to 2100; that is, Sen's Slope is utilized to calculate the trend value, and then the M-K test is utilized to judge the trend significance. The calculation method is as follows:

$$Slope = Median(\frac{x_j - x_i}{j - i}) \tag{10}$$

In the formula, x_j and x_i represent the sequence values of j time and i time, respectively. The positive and negative slope values reflect the change trend of the data, and represent the change rate of the time series data. When the value is positive, the data show an upward trend, and when the value is negative, the data show a downward trend.

$$S = \sum_{i=1}^{n-1} \sum_{j=i+1}^{n} \mathrm{sgn}(x_j - x_i) \tag{11}$$

$$\mathrm{sgn}(x_j - x_i) = \begin{cases} i & x_j - x_i > 0 \\ 0 & x_j - x_i = 0 \\ -1 & x_j - x_i < 0 \end{cases} \tag{12}$$

In the formula, n is the length of the time series, and x_j and x_i are the sequence values at time j and time i, respectively. When the statistic S is approximately equal to the standard normal test statistic Z, it can be used to test the following trend:

$$Z = \begin{cases} \frac{S-1}{\sqrt{Var(S)}} & S > 0 \\ 0 & S = 0 \\ \frac{S+1}{\sqrt{Var(S)}} & S < 0 \end{cases} \tag{13}$$

$$Var(S) = \frac{n(n-1)(2n+5)}{12} \tag{14}$$

That is, when $|Z| > Z_{1-\frac{\alpha}{2}}$, it is considered that the time series trend is significant; otherwise, it is not significant.

In addition, we calculated the relative change rate of rainfall erosivity from 1961 to 2100 to reveal the fluctuation in rainfall erosivity in the Loess Plateau in historical and future periods. Its calculation formula is:

$$A_n = \frac{R_n - M_{1961-1990}}{M_{1961-1990}} \times 100\% \tag{15}$$

Among them, A_n represents the relative change rate of rainfall erosivity in the year n ($1961 \le i \le 2100$); R_n represents the estimated value of rainfall erosivity in the year n; and $M_{1961–1990}$ represents the average value of rainfall erosivity from 1961 to 1990.

2.3.6. Coefficient of Variation (COV)

The coefficient of variation serves as a means to depict the pattern of fluctuations in annual rainfall erosivity. In this paper, the annual rainfall erosivity increment is calculated based on the historical period (1961–2014) and future period (2015–2100) of each pixel. One of its advantages lies in its independence from requiring the average value as a reference, thereby effectively mitigating the impact of measurement scale and dimension. The calculation method is as follows:

$$C_v = \frac{1}{\overline{x}}\sqrt{\frac{\sum_{i=1}^{n}(x_i - \overline{x})^2}{n-1}} \quad (16)$$

In the formula, C_v is the coefficient of variation of annual rainfall erosivity, x_i is the value in the year i, and $\overline{x}$ is the average value of annual rainfall erosivity. The smaller the C_v value, the less fluctuation there is in annual rainfall erosivity, whereas the larger the C_v value, the greater the fluctuations in annual rainfall erosivity.

3. Results

3.1. Evaluation of Precipitation under the Multi-Model Ensemble Mean

The historical period (1961–2014) is divided into two stages in the accuracy evaluation: the delta construction stage (1961–1990) and accuracy verification stage (1991–2014). That is, the simulation data and observation data from 1961 to 1990 were used to calculate the delta (P) according to formula 2. The simulation data spanning from 1961 to 2014 served as the basis for this model, and we obtained the high-resolution data after applying Formula (1) to downscale them.

Table 3 gives the comparison results of three indicators (R^2, MAE, RMSE) for evaluating the precipitation accuracy of 27 GCM models. On the whole, the accuracy of the 27 models after delta downscaling was greatly improved. Before downscaling, the span of R^2 was 0.34–0.79, the span of MAE was 14.55–38.83 mm, and the RMSE span was 21.25–49.00 mm. After downscaling, R^2 ranged from 0.71 to 0.87, MAE ranged from 11.35 to 16.57 mm, and RMSE ranged from 16.70 mm to 29.29 mm. It can be seen that it is feasible to use the delta downscaling method to downscale the low-resolution simulation grid information to a grid with a resolution of 500 m × 500 m.

Table 3. Evaluation of global climate models' monthly precipitation simulation ability in the validation period (1991–2014) of the Loess Plateau.

NAME	R^2			MAE (mm)			RMSE (mm)			Wi	Rank
	Before	After	ERA5	Before	After	ERA5	Before	After	ERA5		
ACCESS-CM2	0.62	0.64	0.66	18.68	15.74	15.84	25.11	24.15	24.49	1.88	21
ACCESS-ESM1-5	0.72	0.73	0.72	18.18	13.95	15.33	22.83	20.8	21.71	13.92	9
AWI-CM-1-1-MR	0.61	0.63	0.66	18.63	16.98	17.74	25.31	24.28	24.58	0.93	25
BCC-CSM2-MR	0.72	0.72	0.68	15.6	14.28	16.47	21.4	20.82	23.49	8.65	13
CAMS-CSM1-0	0.34	0.58	0.65	25.37	18.13	18.29	31.77	27.93	25.83	0	27
CanESM5	0.62	0.65	0.67	23.34	16.6	16.04	31.95	25.22	23.57	1.5	22
CanESM5-1	0.62	0.68	0.66	23.97	16.95	16.99	33.29	25.66	24.32	1.5	23
CAS-ESM2-0	0.58	0.73	0.74	25.75	14.01	15.28	32.75	20.67	21.18	14.74	7
CESM2-WACCM	0.72	0.76	0.72	29.85	14.42	15.58	40.17	21.42	21.99	10.61	11
CMCC-CM2-SR5	0.79	0.79	0.82	38.83	12.68	13.17	49	18.52	18.36	100	1
CMCC-ESM2	0.79	0.81	0.79	34.83	13.71	14.42	44.37	19.37	19.93	60.03	2
EC-Earth3	0.66	0.77	0.67	16.39	14.04	17.50	25.46	18.58	25.62	31.48	4
EC-Earth3-Veg	0.65	0.73	0.72	15.99	14.21	15.47	24.22	20	22.32	14.74	8
EC-Earth-Veg-LR	0.73	0.74	0.71	14.55	13.63	16.41	21.25	19.39	22.41	31.48	5
FGOALS-f3-L	0.65	0.65	0.63	16.24	15.36	17.60	24.81	22.62	25.89	3.48	16
FGOALS-g3	0.65	0.71	0.70	15.62	14.79	16.07	22.73	21.61	22.57	5.26	15
IITM-ESM	0.53	0.62	0.69	21.51	16.41	16.33	27.33	24.99	23.33	1.14	24
INM-CM4-8	0.75	0.76	0.77	31.79	14.01	15.26	39.33	20.58	21.11	18.8	6
INM-CM5-0	0.67	0.68	0.69	31.38	15.59	16.36	39.18	23	23.26	3.48	17
IPSL-CM6A-LR	0.71	0.73	0.74	15.23	14.3	15.78	21.77	19.94	21.50	11.8	10
KACE-1-0-G	0.64	0.65	0.68	17.25	16.29	16.66	24.73	22.99	23.85	2.3	20

Table 3. *Cont.*

NAME	R^2			MAE (mm)			RMSE (mm)			Wi	Rank
	Before	After	ERA5	Before	After	ERA5	Before	After	ERA5		
MIROC6	0.68	0.72	0.73	25.84	14.57	15.53	33.7	21.14	21.53	7.09	14
MPI-ESM1-2-HR	0.53	0.6	0.68	19.6	17.79	18.09	27.2	26.35	24.59	0.25	26
MPI-ESM1-2-LR	0.53	0.66	0.68	23.08	15.52	16.26	29.44	23.88	23.43	2.94	18
MRI-ESM2-0	0.51	0.66	0.56	17.77	16.74	18.65	31.07	22.91	29.74	2.61	19
NorESM2-LM	0.71	0.74	0.73	27.95	14.54	15.49	37.63	21.23	21.20	9.09	12
TaiESM1	0.77	0.8	0.77	29.63	13.47	14.75	38.81	19.48	20.28	52.63	3
MME	0.89	0.93	0.87	20.97	11.03	12.12	26.79	15.88	16.52	×	×

Comparing the three evaluation indicators, CMCC-CM2-SR5 and CMCC-ESM2 hold the top two positions in the rankings, TaiESM1 and EC-Earth3 rank slightly differently in RMSE (R^2 and MAE are ranked third, while RMSE is ranked fourth and third, respectively), and EC-Earth-Veg-LR and INM-CM4-8 are steadily ranked fifth and sixth. The rankings of ACCESS-ESM1-5, CAS-ESM2-0, and IPSL-CM6A-LR are not stable. As an independent meteorological data set, the ERA5 reanalysis data set was used to compare the accuracy with the downscaled data set in this paper. The downscaled data set after the multi-mode set was compared with the ERA5. The R^2 was 0.87, the MAE was 12.12 mm, and the RMSE was 16.52 mm. Compared with ERA5, the results show that the reliability of using the downscaled data to further predict the future rainfall erosivity change is high, which can reasonably reflect future climate change predictions under the assumption of specific emission scenarios in the future, which are affected by the external forcing of climate systems such as anthropogenic greenhouse gas emissions.

Using Formula (7) to calculate the comprehensive scores of the three indicators, the 10 models suitable for rainfall-related research in the Loess Plateau were CMCC-CM2-SR5, CMCC-ESM2, TaiESM1, EC-Earth3, EC-Earth-Veg-LR, INM-CM4-8, CAS-ESM2-0, EC-Earth-Veg, ACCESS-ESM1-5, and IPSL-CM6A-LR.

Table 3 also shows the simulated values under the multi-model set. The improvement in MME data accuracy is evident when considering the three evaluation criteria: R^2, MAE, and RMSE. Figure 2 shows the comparison of 27 GCM models, MME, CN, and ERA5. The figure illustrates that in comparison to the observed data (CN and ERA5), the output from the original GCM exhibits an overestimation of nearly twice the amount, and the monthly bias results with more precipitation are more significant. The downscaling outcomes from the multi-model ensemble align well with the observed data, which greatly corrects the output deviation of the GCM model and can be used for future precipitation predictions on the Loess Plateau.

Figure 3 is the result of comparative analysis of the spatial characteristics of precipitation. The errors of the GCM results were mainly concentrated in the southern part and mainly manifested in the overestimation of rainfall and the expansion of the range of variation. The error of the simulated precipitation grid data obtained by the MME method was basically corrected, and it showed good correspondence with the CN data in space. The southern region with large errors can also be accurately displayed. In summary, using the multi-model ensemble method, we gathered simulation data from 10 models chosen through the evaluation system, and the simulated rainfall data obtained can be used for the future prediction of rainfall in the Loess Plateau.

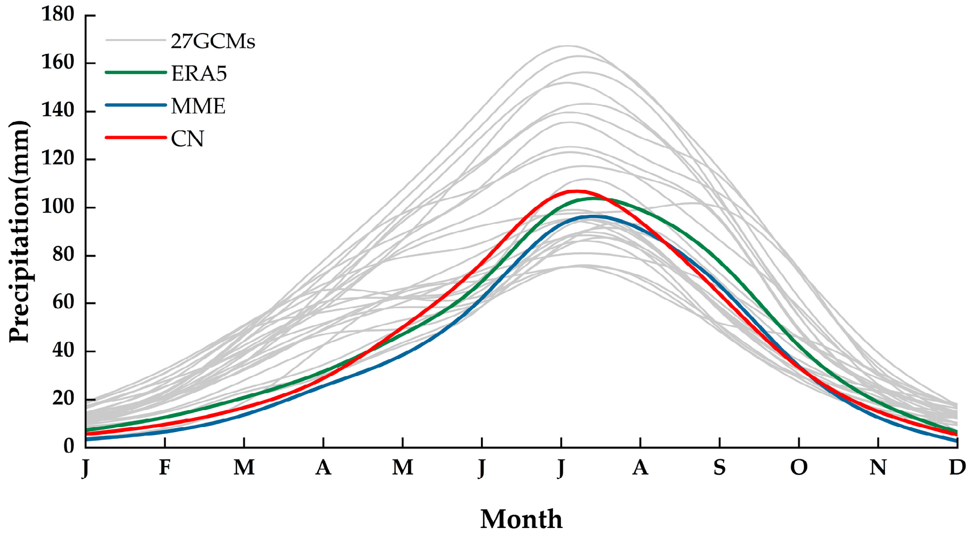

Figure 2. Comparison results of the annual precipitation under a multi-model ensemble (MME) from January 1991 to December 2014 on the Loess Plateau. (In this graph, the gray line stands for the data before downscaling of the 27 GCM data sets used in this paper, the red line stands for the observed precipitation data, the blue one stands for the multi-model ensemble data of the 10 models selected above, and the green line stands for ERA5 data).

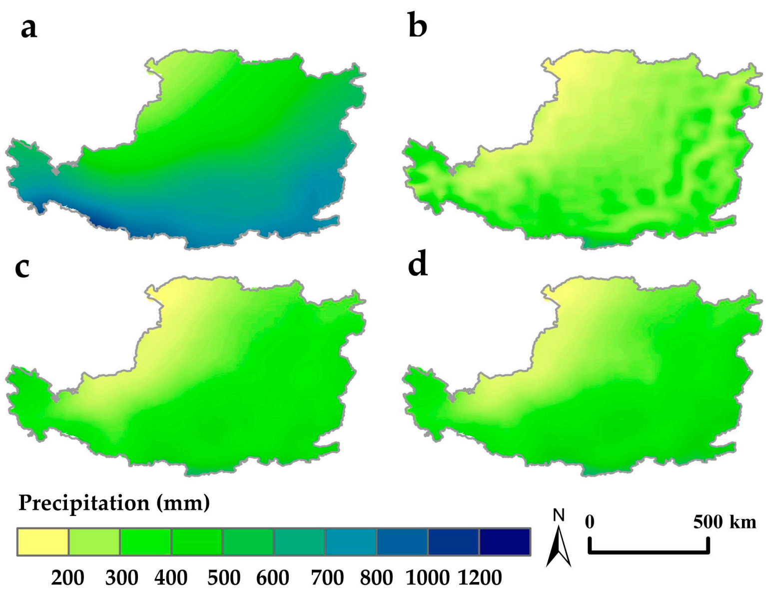

Figure 3. The findings from the comparison of spatial distribution characteristics of precipitation during the validation period (1990–2014) ((**a**) represents the original GCM data, (**b**) represents the ERA5 data, (**c**) represents the observed precipitation data, and (**d**) represents the multi-model ensemble data).

3.2. Characteristics of Rainfall Erosivity from 1961 to 2014

We can observe the changes in annual rainfall erosivity during 1961–2014 in Figure 4. The average annual rainfall erosivity of the Loess Plateau was 1259.64 MJ·mm·hm^{-2}·h^{-1}. The maximum was 2356.23 MJ·mm·hm^{-2}·h^{-1}, which appeared in 1963, and the minimum value was 569.39 MJ·mm·hm^{-2}·h^{-1}, which appeared in 1991. The amplitude was 1786.84 MJ·mm·hm^{-2}·h^{-1}. Linear fitting revealed that the overall performance showed a slow downward trend, with a decline rate of −3.54 MJ·mm·hm^{-2}·h^{-1}·a^{-1}.

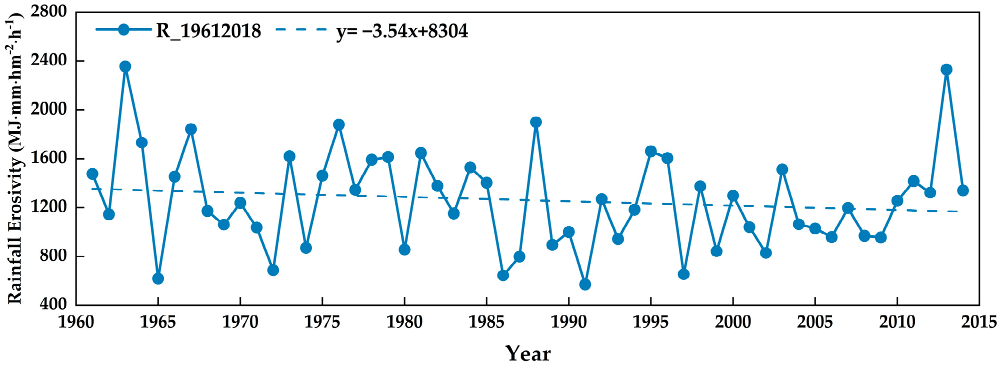

Figure 4. Rainfall erosivity evolution during 1961–2014.

Overall, the average annual rainfall erosivity of the Loess Plateau showed significant spatial differences. It showed a declining trend, which mainly accounted for 41.89% of the total, and was widely distributed in most areas of Inner Mongolia, Yulin, Weinan, Yan'an, Yinchuan, Wuzhong City, and eastern Gansu. There was a significant downward trend accounting for 0.04% of the overall area. The distribution sites were mainly concentrated in most areas of Shanxi Province, most areas of Henan Province, Pingliang City, and Changzhi City. The proportion of annual rainfall erosivity changes showing an upward trend for many years was 58.11%, mainly distributed in the whole region of Qinghai Province, western Gansu Province, most areas of Shaanxi Province, Lyuliang City, Shanxi Province, Sanmenxia City, Henan Province, and Luoyang City; 3.55% of the total area experienced a substantial rise in annual rainfall erosivity, mainly distributed in northwestern Ningxia, Yulin City, and Yan'an City.

The coefficient of variation of rainfall erosivity from 1961 to 2014 was calculated pixel by pixel, and the analysis diagram shown in Figure 5b was obtained. On the whole, the proportion of medium fluctuation change was the highest, accounting for 46.71%, followed by relatively low fluctuation, accounting for 38.29%. The low fluctuation changes were mainly distributed in the whole region of Qinghai Province, Lanzhou City, Tianshui City, Gansu Province, Dingbian County, and Shaanxi Province; the relatively low fluctuations were mainly distributed in most areas of Gansu Province, southern Ningxia, Ordos City in Inner Mongolia, northwestern and southeastern Shaanxi Province, Ordos City in Inner Mongolia, northwestern and southeastern Shaanxi Province, most areas of Henan Province, Taiyuan City in Shanxi Province, Yuncheng City, and so on. The medium fluctuation changes were mainly distributed in most areas of northern and central Shanxi Province, Inner Mongolia, northern Ningxia, and central Shaanxi Province; the relatively high fluctuation changes were mainly distributed in Pingluo County of Ningxia, Shuozhou City of Shanxi, Yangquan City, Changzhi City, Yan'an City of Shaanxi Province, Yulin City, etc. The high fluctuation changes were concentrated in Puyang County, Pingding County, and Shun County in Shanxi Province. The coefficient of variation indicates the spatial fluctuation degree of rainfall erosivity. Compared with the slope change analysis chart, the medium fluctuation is mostly positive.

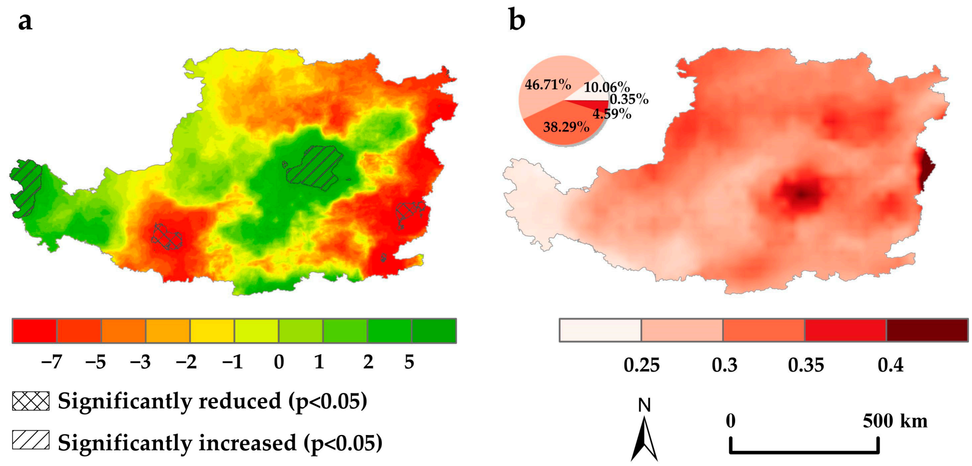

Figure 5. Characteristics of changes in rainfall erosivity from 1961 to 2014. (Panel (**a**) represents the spatial distribution of the change rate of annual rainfall erosivity from 1961 to 2014, unit: MJ·mm·hm^{-2}·h^{-1}·a^{-1}; panel (**b**) represents the spatial distribution of C_v and the proportion of each fluctuation degree.)

3.3. Estimation of the Future Rainfall Erosivity

The relative change rate of annual rainfall erosivity relative to the base period (1961–1990) during 1961–2100 is shown in Figure 6. In the future period (2015–2100), the relative rate of change under the four SSP scenarios fluctuates between −46.23~42.23%, −39.81~53.43%, −34.67~67.02%, and −35.13~81.80%, and the average annual rainfall erosivity growth rate is between −5.19% and 5.15%. The maximum growth under each scenario appears in 2071, 2064, 2040, and 2077, and the minimum growth under each scenario appears in 2043, 2020, 2050, and 2026. In contrast, the intensity of fluctuations is more pronounced in the SSP5-8.5 scenario.

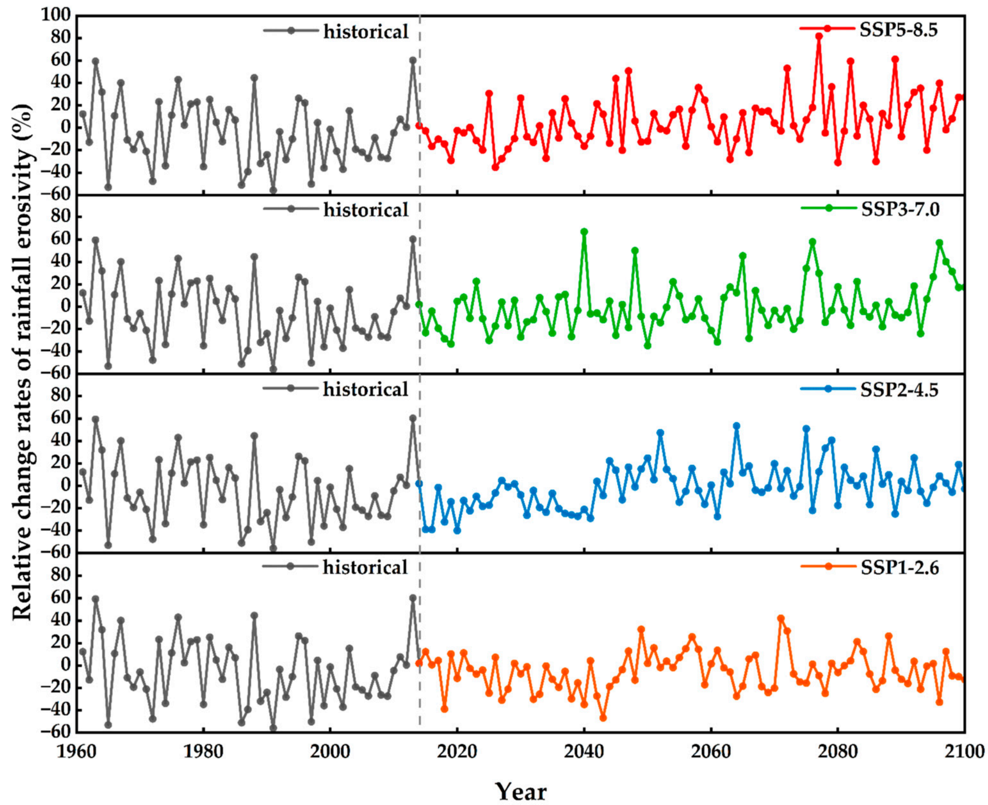

Figure 6. Relative changes in rainfall erosivity during 1961–2100 in different scenarios.

Using the analysis method introduced in Section 2.3.5, the change rate of rainfall erosivity and the significance analysis results are obtained (Figure 7). On the whole, under different scenario simulations, rainfall erosivity shows obvious spatial differences. In the SSP1-2.6 scenario, the change rate is between −3.29 and 6.08 MJ·mm·hm^{-2}·h^{-1}·a^{-1}. There was a decline in the annual rainfall erosivity, which constituted 41.89% of the total. This decline was observed extensively in the northern section of the study area and Jinzhong City, Shanxi Province. Among them, there is a significant downward trend, accounting for 0.04% of the overall area, and the distribution is mainly concentrated in Ordos City, Inner Mongolia. The proportion of annual rainfall erosivity changes, showing an upward trend of 58.11%, mainly distributed in the southern part and Dalad Banner and Tumed Right Banner in Inner Mongolia. An area demonstrating a noteworthy increase in annual rainfall erosivity constituted 3.55% of the total land area. This increase was primarily observed in the same city and Guide County of Qinghai Province and the southern region of Shaanxi Province.

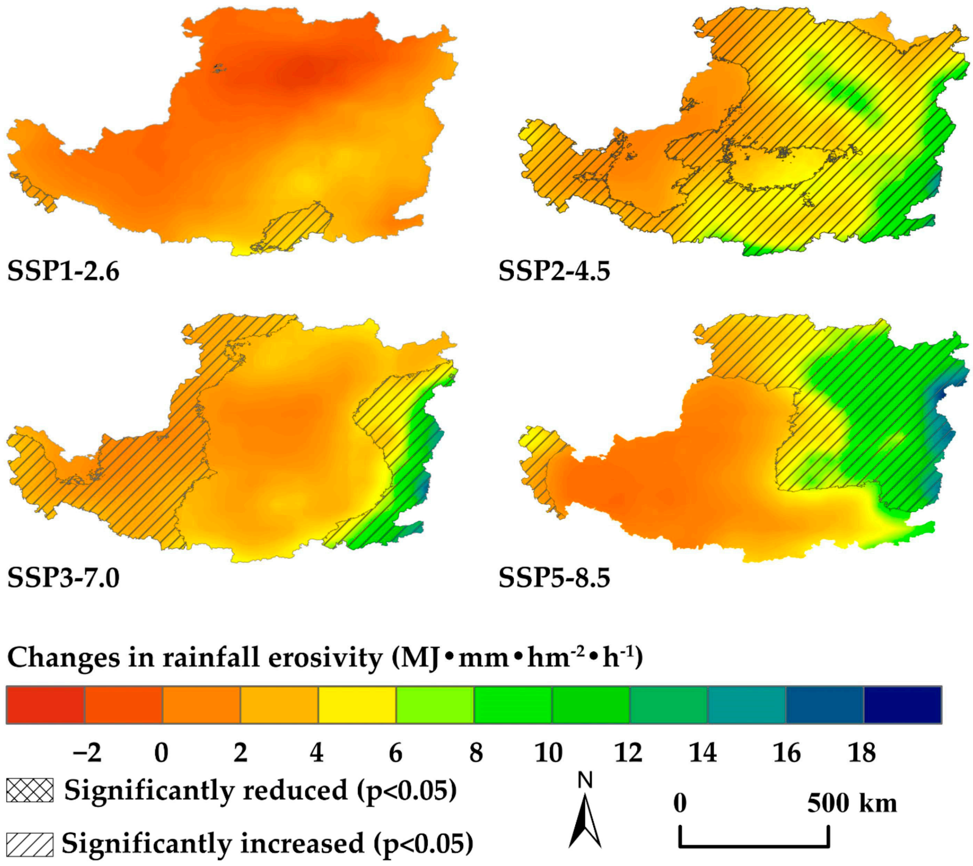

Figure 7. Spatial distribution of changes in rainfall erosivity under different scenarios from 2015 to 2100. (the oblique line area represents a significant increase area, and the network line area represents a significant decrease area).

Under the SSP2-4.5 scenario, the change rate is between 0.39 and 16.94 with no downward trend. The area showing a significant upward trend accounts for 71.58% of the total area. A large area is distributed throughout the study area, mainly concentrated in the provinces: Shanxi Province, Inner Mongolia, Qinghai, and Shaanxi. Under the SSP3-7.0 scenario, the change rate is between 0.39 and 19.25. The overall trend in the annual rainfall erosivity of the Loess Plateau was characterized by an increase, and there was no downward trend. The area showing a significant upward trend comprised 41.38%. It is mainly distributed in Qinghai Province, Gansu Province and most parts of Ningxia, Ordos City, Inner Mongolia, eastern Shanxi Province, and Henan Province. Under the SSP585 scenario, the rate of change is between −0.53 and 20.15. The annual rainfall erosivity showed a downward trend, mainly accounting for 9.44% of the overall and mainly concentrated in Minhe Hui Autonomous County of Qinghai Province, southern Ningxia, and Baoji City of Shaanxi Province. The above sites showed an insignificant downward trend. The proportion of annual rainfall erosivity changes showing an upward trend was 90.56%, mainly distributed in the whole study area except Gansu Province. The region experiencing a substantial rise in annual rainfall erosivity accounted for 49% of the entire study area, mainly concentrated in northern Inner Mongolia, northern and central Shaanxi Province, most of Shanxi Province, and western Qinghai Province.

Through comparison, it was found that under the background of climate change, the increase in rainfall erosivity is a universal law, but there are obvious spatial differences in its trend intensity, which is particularly significant under the SSP5-8.5 scenario, and shows a significant increasing trend in a large area in the eastern part of the study area.

3.4. Analysis of Variability

According to Formula (16), the coefficient of variation (C_v) for annual rainfall erosivity in the study area was calculated on a pixel-by-pixel basis from 2015 to 2100, and the results are shown in Figure 8. The average coefficients of variation were 0.29 under SSP1-2.6, 0.32, 0.33, and 0.32, respectively. According to the size of C_v, it was divided into five levels, namely low fluctuation change ($C_v < 0.25$), relatively low fluctuation change ($0.25 < C_v < 0.3$), medium fluctuation change ($0.3 < C_v < 0.35$), relatively high fluctuation change ($0.35 < C_v < 0.4$), and high fluctuation change ($C_v > 0.4$). It can be seen from Figure 6 that the fluctuation law of annual rainfall erosivity reflected by C_v in different scenarios is also different.

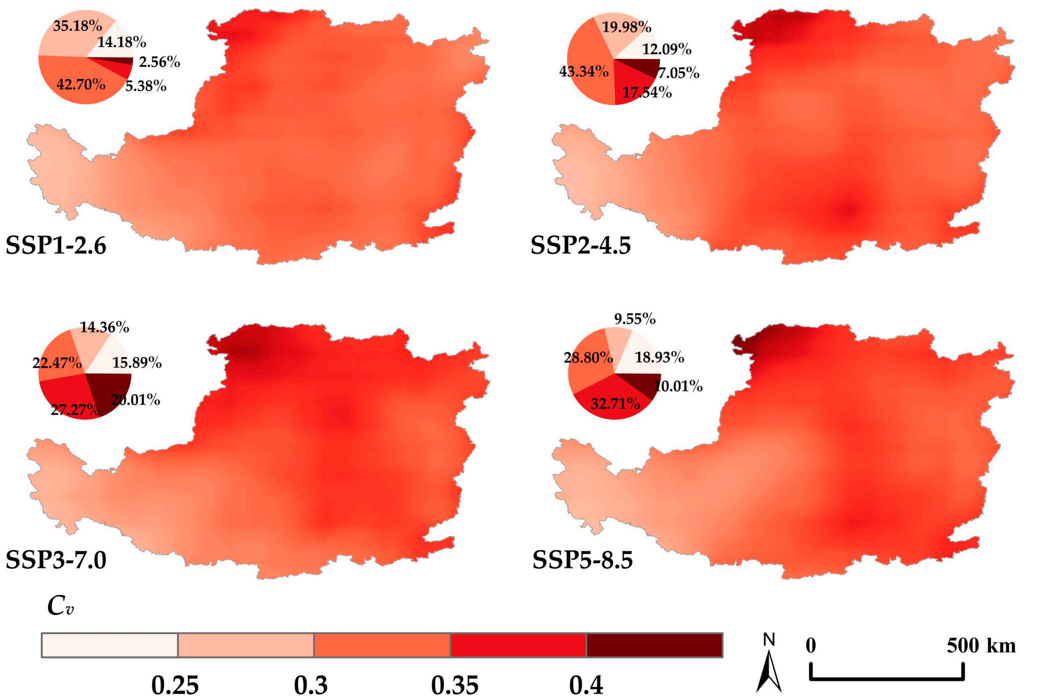

Figure 8. The changes in C_v under various scenarios from 2015 to 2100 in their spatial distribution. (The pie chart represents the proportion of each fluctuation degree.)

In the SSP1-2.6 scenario, the highest proportion pertains to medium fluctuation changes, accounting for 42.70%, followed by relatively low fluctuation, accounting for 35.18%. The low fluctuation change is mainly distributed in the whole region of Qinghai Province, Datong City of Shanxi Province, and most areas of Gansu Province. Relatively low fluctuations are mainly distributed in northern Ningxia, southern Shaanxi, and central

Shanxi. Southeastern and central parts of Inner Mongolia, most areas of Shaanxi Province, and eastern Shanxi are the primary areas characterized by medium fluctuation changes; the relatively high fluctuation changes are mainly distributed in Hangjin Banner of Inner Mongolia, Changzhi City of Shanxi Province, and Zhengzhou City of Henan Province; high fluctuation changes are concentrated in Hangjinhou Banner, Bayanhaier City, and the Inner Mongolia Autonomous Region.

In the SSP2-4.5 scenario, the medium fluctuation change accounts for the highest proportion, accounting for 43.37% of the area, followed by the relatively low fluctuation, accounting for 19.98%. The low fluctuation changes are mainly distributed in the whole region of Qinghai Province and most areas of Gansu Province; the relatively low fluctuations are mainly distributed in the Ordos City of Inner Mongolia, the northern part of Shaanxi, the Linzhou City of Shanxi Province, Datong City, and Jinzhou City; the medium fluctuation changes are mainly distributed in the Otog Banner of Ordos City in Inner Mongolia, the northwest of Shanxi Province, Wuzhong City in Ningxia, Zhongwei City, and the southwest and central part of Shanxi Province; the relatively high fluctuation changes are mainly distributed in the south of Gansu, the middle of Shaanxi, and the middle of Inner Mongolia. High fluctuation changes are concentrated in northern Inner Mongolia and Weinan City, Shaanxi Province.

In the SSP3-7.0 scenario, the proportion of relatively low fluctuations is the highest, accounting for 27.27% of the area, followed by moderate fluctuations, accounting for 22.47%. Low fluctuation changes are mainly distributed in southern Ningxia, Qinghai Province, and most areas of Gansu Province. The relatively low fluctuations are mainly distributed in Ningxia, Baiyin City of Gansu Province, most of Shanxi Province, and Taiyuan City of Shanxi Province. The medium fluctuation changes are mainly distributed in the southern part of Inner Mongolia, Shaanxi, and most of Shanxi. The relatively high fluctuation changes are mainly distributed in most areas of Shanxi Province, western Shanxi and southern Ordos City, Inner Mongolia. High fluctuation changes are concentrated in most areas of Inner Mongolia and Yulin City, Shaanxi Province.

Under the SSP5-8.5 scenario, the area with relatively low fluctuation changes held the largest share, representing 32.71% of the total area, followed by medium fluctuation, accounting for 28.80%. The low fluctuation changes are mainly distributed in the whole region of Qinghai Province, all regions except Baiyin City in Gansu Province, and the central region of Ningxia. Relatively low fluctuations are mainly distributed in Wuzhong City, Yinchuan City, and western Shaanxi Province. The medium fluctuation changes are mainly distributed in the southern part of Inner Mongolia and central Shaanxi Province. Predominantly, the regions marked by relatively high fluctuation changes are situated in the central and southern parts of Inner Mongolia, Yulin, Yan’an, Linfen, and Shuozhou in Shaanxi Province; the high fluctuation changes are concentrated in Hangjinhou Banner, Bayanhaier City in Inner Mongolia, Weinan City in Shaanxi, and Zhengzhou City in Henan Province.

The coefficient of variation expresses the fluctuation degree of long-term rainfall erosivity change. Compared with the slope change image, it can be seen that the changes of Shanxi Province with medium fluctuation and Inner Mongolia and Shaanxi Province with high fluctuation are positive.

4. Discussion

The Loess Plateau is one of the most severe soil-erosion and ecologically fragile areas in China and even in the world. Water erosion is the main form of soil erosion here. Since 1999, efforts to control soil erosion on the Loess Plateau have continuously increased, resulting in a notable decline in soil erosion intensity and a substantial reduction in sediment entering the Yellow River. Some progress has been made in comprehensive control of soil erosion [61,62]. Despite efforts to mitigate soil erosion, water erosion continues to be a persistent challenge on the Loess Plateau.

The spatial and temporal changes in rainfall erosivity in various river systems are significantly associated with global climate change. When the temperature rises and the evaporation is strong, the spatial pattern of atmospheric circulation and precipitation is readjusted on a global scale, and the humidity increases, which leads to changes in rainfall and the rainfall intensity of external erosion force [63]. The Loess Plateau is situated on China's second ladder. It is restricted by latitude, longitude, and topography, which makes its climate change complex and rainfall changes violent.

The Loess Plateau sees concentrated rainfall periods during the year, which leads to prominent soil erosion problems caused by rainfall. Therefore, we focused on the Loess Plateau and selected ten GCM models from the latest released CMIP6 multi-model data using a multi-model ensemble method. By using the delta downscaling method, this study simulated the changes in rainfall erosivity from 1990 to 2009 as the baseline period, and generated scenarios of rainfall erosivity changes during 2015–2100. There are many methods for calculating rainfall erosivity, and the initial research was mostly based on the rainfall intensity and rainfall kinetic energy to estimate rainfall erosivity. But obtaining long-term rainfall process data is hard work, which limits the application of this method. In 2003, Zhang et al. [60] established a method for estimating rainfall erosivity based on different types of rainfall data, which provided a methodological basis for assessing rainfall erosivity using conventional rainfall statistics. The method proposed by Zhang et al. has been widely used in the Loess Plateau [64,65]. The model of calculating rainfall erosivity using monthly rainfall data is based on the loess area, and it is verified by the accuracy of the measured site rainfall data. The coefficient of determination is 0.861 and the relative error is 0.321. Combined with the monthly data of 4776 periods from 1961 to 2100 used in this paper, the region's rainfall erosivity was determined to use a monthly rainfall erosivity model.

Compared with existing studies, utilizing daily precipitation data from 1961 to 2017 and downscaled precipitation estimates obtained from five selected global climate models under the RCP4.5 medium-emission scenario, Gao et al. [66] conducted a thorough analysis to examine the spatiotemporal variation in rainfall erosivity within the Yellow River Basin. Gao et al. [66] believed that due to the increasing number of erosive rainfall days, the relative rate of change was 13.6% and 19.5%, while the conclusion of this study was 13.48–25.56%. Studies have shown that CMIP6 precipitation prediction is slightly higher than CMIP5 precipitation, because CMIP5 and CMIP6 simulation parameters are different, CMIP6 is more accurate in predicting rainfall [67]. The findings suggest that predicting future climate change is essential because rainfall erosivity under different scenarios varies in time and space.

Based on CMIP5 simulation data, Panagos et al. [5] predicted the changes of annual rainfall erosivity under three RCP concentrations in 2041–2060 and 2061–2080. According to the results, the global average annual rainfall erosivity varied between 2765 and 2822 MJ·mm·hm^{-2}·h^{-1} by the year 2050 and between 2782 and 2942 by 2070. Takhellambam et al. [3] analyzed the evolution of annual rainfall erosivity in the southeastern United States based on five CMIP6 data sets, and concluded that the annual rainfall erosivity in the southeastern United States will increase by 27% from 2030 to 2059. Combined with the conclusion of this paper, the average annual rainfall erosivity on the Loess Plateau during 2041–2060 is 1147.38–1360.97 MJ·mm·hm^{-2}·h^{-1}·a^{-1}, and it is 1255.27–1430.79 MJ·mm·hm^{-2}·h^{-1}·a^{-1} during 2061–2080. The annual rainfall erosivity of the Loess Plateau will increase by 26% to 32% from 2030 to 2059. In combination, the annual rainfall erosivity of the Loess Plateau in China will be lower than the global average erosivity in the future, and higher than that of the United States. Consistent with the above research, the annual rainfall erosivity will show an upward trend, and will increase by 40.18~61.20% during 2080–2100, which is not analyzed in the above literature. The increase of rainfall erosivity may cause the existing soil and water conservation projects to fail to play their original role, and even cause a certain degree of damage in the future. Therefore, we should continue to strengthen the maintenance of existing methods and the introduction of new methods, as soil erosion prevention is still arduous. Especially in the northeast, while annual rainfall erosivity in this region exhibits fluctuations in future projections, the overarching trend is one of growth. The increase in annual rainfall erosivity will unquestionably augment the challenge of soil erosion management. It is necessary to strengthen and prevent protection measures.

In light of the complex nature of climate change in high-altitude regions and the inherent limitations of climate models, uncertainties persist in accurately predicting climate change scenarios. Efforts to enhance the reliability of multi-model ensemble projections rely on the precision of General Circulation Model (GCM) data and accurate simulation of future human activities. From the analysis in this study, we find that improving the model resolution can indeed improve the model performance to some extent, especially in the spatial distribution of precipitation, where its effects are significant. All models can reproduce the characteristics of precipitation in the study area, but there are still systematic biases compared to observations. When comparing the simulation of a single model to the multi-model ensemble mean, it can be observed that the latter yields more accurate estimations of monthly precipitation, aligning closely with the actual observations.

Because of the intricate nature of high-altitude climate change and the inherent limitations of climate models, uncertainties persist in climate change projections. Future research will focus on integrating multiple assessment approaches and downscaled methods to achieve more precise and comprehensive climate change scenario projections, particularly in high-altitude regions. It is necessary to obtain more simulation results from models in the CMIP6 comparison project in the future, and further evaluate precipitation predictions in the Loess Plateau region from multiple climate models combined with the measured stations. Furthermore, we observe a declining trend in rainfall erosivity from 1961 to 2014 during the historical period. This is a good phenomenon for controlling soil loss. With the increase of vegetation coverage in the Loess Plateau, the erosion damage of rainfall to the surface can be greatly reduced [68]. However, combined with the conclusions of this study, rainfall erosivity will increase to varying degrees under different climate change scenarios in the future, and it will continue to increase. This undoubtedly poses a greater challenge to soil erosion control. Consequently, there is a need to reinforce medium- and long-term land use planning and consistently enhance prevention, protection, and supervision efforts. Rainfall erosivity, as the main climatic factor used to measure soil erosion, is related to rainfall parameters such as rainfall and rainfall intensity. In forthcoming research, we intend to focus more on assessing the impact of extreme climate events and rainfall intensity on rainfall erosivity.

5. Conclusions

In this study, we utilized simulation data from 27 models within the recently released CMIP6 initiative. From this tool, we selected 10 models of preference to assess the variations in rainfall erosivity on the Loess Plateau spanning from 1961 to 2100. The principal findings can be summarized as follows:

Among the 27 GCM models used in this paper, the most suitable climate models for simulating monthly precipitation in the Loess Plateau in the future were CMCC-CM2-SR5, CMCC-ESM2, TaiESM1, EC-Earth3, EC-Earth-Veg-LR, INM-CM4-8, CAS-ESM2-0, EC-Earth-Veg, ACCESS-ESM1-5, and IPSL-CM6A-LR.

In the historical period (1961–2014), the Loess Plateau experienced a decline in annual rainfall erosivity, constituting 41.89% of the total area. Notably, a significant reduction trend encompassed 0.04% of the total area. The proportion of annual rainfall erosivity changes showing an upward trend for many years was 58.11%, and the area with a significant increase in annual rainfall erosivity accounted for 3.55% of the total area, mainly distributed in northwestern Ningxia, Yulin, and Yan'an. As far as the numerical change of annual rainfall erosivity is concerned, the average annual rainfall erosivity in the historical period of the Loess Plateau is 1259.64 $\mathrm{MJ \cdot mm \cdot hm^{-2} \cdot h^{-1}}$, which decreases slowly at a rate of $-3.54\ \mathrm{MJ \cdot mm \cdot hm^{-2} \cdot h^{-1} \cdot a^{-1}}$. Through the collaborative analysis of change rate and coefficient of variation, it was found that the relatively low fluctuation and low fluctuation of rainfall erosivity in the study area accounted for 56.58% of the study area from 1961 to 2014, and the changes in Qinghai Province, Gansu Province, and Shaanxi Province were positive, and the change in annual rainfall erosivity continued to maintain an increasing trend.

In the future period (2015–2100), the annual rainfall erosivity will change over time. The annual rainfall erosivity of the Loess Plateau showed a downward trend, mainly accounting for 41.89%, 0%, 0%, and 9.44% of the whole, and the proportion of annual rainfall erosivity changes over the years showed upward trends of 58.11%, 100%, 100%, and 90.56%. In terms of the change of annual rainfall erosivity, the annual rainfall erosivity of the Loess Plateau will increase by 13.48–25.86% in the future, with a change rate between 0.7 and 4.71, and the annual rainfall erosivity will maintain an increasing trend, especially under the SSP5-8.5 scenario. In terms of spatial distribution, most areas showed an increasing trend. Among them, most areas of Shanxi Province, central Shaanxi, and Inner Mongolia increased greatly, which was not conducive to soil and water conservation and ecological environment construction on the Loess Plateau. Through the collaborative analysis of change rate and coefficient of variation, it is found that the relatively low fluctuation and low fluctuation of rainfall erosivity in the study area under different scenarios account for 49.36%, 32.07%, 30.25%, and 28.38% of the study area, respectively, and the changes in Qinghai Province, Gansu Province, and Ningxia are positive, and the change of annual rainfall erosivity continues to maintain an increasing trend.

Author Contributions: Conceptualization: X.L. and P.X.; data curation: X.L.; formal analysis: X.L., P.X. and Z.W.; funding acquisition: P.X.; investigation: S.H.; methodology: X.L. and P.X.; project administration: P.X. and S.H.; resources: X.L. and Z.W.; software: X.L.; supervision: X.L. and P.X.; validation: X.L. and Z.W.; visualization: Z.W.; writing—original draft: X.L. and P.X.; writing—review and editing: X.L., P.X., S.H. and Z.W. All authors have read and agreed to the published version of the manuscript.

Funding: This research was funded by the National Natural Science Foundation of China for Yellow River Water Science (U2243210), and the National Key Research and development project (2022YFF1300805).

Data Availability Statement: The CMIP6 monthly data are available at https://esgf-index1.ceda.ac.uk/search/cmip6-ceda/, accessed on 22 March 2023. The ERA5 monthly data are available at https://cds.climate.copernicus.eu/cdsapp#!/dataset/reanalysis-era5-single-levels?tab=form, accessed on 22 March 2023. The CN05.1 daily data are available at https://data.cma.cn/, accessed on 22 March 2023.

Conflicts of Interest: The authors declare no conflicts of interest.

References

1. Yang, X.; Yang, Q.; Zhu, H.; Wang, L.; Wang, C.; Pang, G.; Du, C.; Mubeen, M.; Waleed, M.; Hussain, S. Quantitative Evaluation of Soil Water and Wind Erosion Rates in Pakistan. *Remote Sens.* **2023**, *15*, 2404. [CrossRef]
2. Amundson, R.; Berhe, A.A.; Hopmans, J.W.; Olson, C.; Sztein, A.E.; Sparks, D.L. Soil and Human Security in the 21st Century. *Science* **2015**, *348*, 1261071. [CrossRef]
3. Takhellambam, B.S.; Srivastava, P.; Lamba, J.; McGehee, R.P.; Kumar, H.; Tian, D. Projected Mid-Century Rainfall Erosivity under Climate Change over the Southeastern United States. *Sci. Total Environ.* **2023**, *865*, 161119. [CrossRef]
4. Grillakis, M.G.; Polykretis, C.; Alexakis, D.D. Past and Projected Climate Change Impacts on Rainfall Erosivity: Advancing Our Knowledge for the Eastern Mediterranean Island of Crete. *CATENA* **2020**, *193*, 104625. [CrossRef]
5. Panagos, P.; Borrelli, P.; Matthews, F.; Liakos, L.; Bezak, N.; Diodato, N.; Ballabio, C. Global Rainfall Erosivity Projections for 2050 and 2070. *J. Hydrol.* **2022**, *610*, 127865. [CrossRef]
6. Zhang, S.; Chen, Y.; Zhou, X.; Zhang, Y. Climate and Human Impact Together Drive Changes in Ecosystem Multifunction-ality in the Drylands of China. *Appl. Soil Ecol.* **2024**, *193*, 105163. [CrossRef]
7. Papalexiou, S.M.; Montanari, A. Global and Regional Increase of Precipitation Extremes Under Global Warming. *Water Resour. Res.* **2019**, *55*, 4901–4914. [CrossRef]
8. Neelin, J.D.; Sahany, S.; Stechmann, S.N.; Bernstein, D.N. Global Warming Precipitation Accumulation Increases above the Current-Climate Cutoff Scale. *Proc. Natl. Acad. Sci. USA* **2017**, *114*, 1258–1263. [CrossRef] [PubMed]

9. Guhathakurta, P.; Sreejith, O.P.; Menon, P.A. Impact of Climate Change on Extreme Rainfall Events and Flood Risk in India. *J. Earth Syst. Sci.* **2011**, *120*, 359–373. [CrossRef]
10. Li, Z.; Zheng, F.; Liu, W.; Flanagan, D.C. Spatial Distribution and Temporal Trends of Extreme Temperature and Precipitation Events on the Loess Plateau of China during 1961–2007. *Quat. Int.* **2010**, *226*, 92–100. [CrossRef]
11. Hoomehr, S.; Schwartz, J.S.; Yoder, D.C. Potential Changes in Rainfall Erosivity under GCM Climate Change Scenarios for the Southern Appalachian Region, USA. *CATENA* **2016**, *136*, 141–151. [CrossRef]
12. Wang, W.; Yin, S.; Gao, G.; Papalexiou, S.M.; Wang, Z. Increasing Trends in Rainfall Erosivity in the Yellow River Basin from 1971 to 2020. *J. Hydrol.* **2022**, *610*, 127851. [CrossRef]
13. Chang, Y.; Lei, H.; Zhou, F.; Yang, D. Spatial and Temporal Variations of Rainfall Erosivity in the Middle Yellow River Basin Based on Hourly Rainfall Data. *CATENA* **2022**, *216*, 106406. [CrossRef]
14. Xu, X.; Yan, Y.; Dai, Q.; Yi, X.; Hu, Z.; Cen, L. Spatial and Temporal Dynamics of Rainfall Erosivity in the Karst Region of Southwest China: Interannual and Seasonal Changes. *CATENA* **2023**, *221*, 106763. [CrossRef]
15. Kilic, O.M.; Gunal, H. Spatial-Temporal Changes in Rainfall Erosivity in Turkey Using CMIP5 Global Climate Change Scenario. *Arab. J. Geosci.* **2021**, *14*, 1079. [CrossRef]
16. Panagos, P.; Ballabio, C.; Meusburger, K.; Spinoni, J.; Alewell, C.; Borrelli, P. Towards Estimates of Future Rainfall Erosivity in Europe Based on REDES and WorldClim Datasets. *J. Hydrol.* **2017**, *548*, 251–262. [CrossRef] [PubMed]
17. Zhu, Q.; Yang, X.; Ji, F.; Liu, D.L.; Yu, Q. Extreme Rainfall, Rainfall Erosivity, and Hillslope Erosion in Australian Alpine Region and Their Future Changes. *Int. J. Climatol.* **2020**, *40*, 1213–1227. [CrossRef]
18. Li, D.; Qi, Y.; Zhou, T. Changes in Rainfall Erosivity over Mainland China under Stabilized 1.5 °C and 2 °C Warming Futures. *J. Hydrol.* **2021**, *603*, 126996. [CrossRef]
19. Mondal, A.; Khare, D.; Kundu, S. Change in Rainfall Erosivity in the Past and Future Due to Climate Change in the Central Part of India. *Int. Soil Water Conserv. Res.* **2016**, *4*, 186–194. [CrossRef]
20. Tebaldi, C.; Debeire, K.; Eyring, V.; Fischer, E.; Fyfe, J.; Friedlingstein, P.; Knutti, R.; Lowe, J.; O'Neill, B.; Sanderson, B.; et al. Climate Model Projections from the Scenario Model Intercomparison Project (ScenarioMIP) of CMIP6. *Earth Syst. Dynam.* **2021**, *12*, 253–293. [CrossRef]
21. Xin, X.; Wu, T.; Zhang, J.; Yao, J.; Fang, Y. Comparison of CMIP6 and CMIP5 Simulations of Precipitation in China and the East Asian Summer Monsoon. *Int. J. Climatol.* **2020**, *40*, 6423–6440. [CrossRef]
22. Diaz-Nieto, J.; Wilby, R.L. A Comparison of Statistical Downscaling and Climate Change Factor Methods: Impacts on Low Flows in the River Thames, United Kingdom. *Clim. Change* **2005**, *69*, 245–268. [CrossRef]
23. Mosier, T.M.; Hill, D.F.; Sharp, K.V. 30-Arcsecond Monthly Climate Surfaces with Global Land Coverage: 30-ARCSECOND Global Climate Surfaces. *Int. J. Climatol.* **2014**, *34*, 2175–2188. [CrossRef]
24. Fan, X.; Jiang, L.; Gou, J. Statistical Downscaling and Projection of Future Temperatures across the Loess Plateau, China. *Weather Clim. Extrem.* **2021**, *32*, 100328. [CrossRef]
25. Peng, S.; Gang, C.; Cao, Y.; Chen, Y. Assessment of Climate Change Trends over the Loess Plateau in China from 1901 to 2100: Assessment of Climate Change Trends over the Loess Plateau. *Int. J. Clim.* **2018**, *38*, 2250–2264. [CrossRef]
26. O'Neill, B.C.; Tebaldi, C.; van Vuuren, D.P.; Eyring, V.; Friedlingstein, P.; Hurtt, G.; Knutti, R.; Kriegler, E.; Lamarque, J.-F.; Lowe, J.; et al. The Scenario Model Intercomparison Project (ScenarioMIP) for CMIP6. *Geosci. Model Dev.* **2016**, *9*, 3461–3482. [CrossRef]
27. Wu, J.; Gao, X.; Giorgi, F.; Chen, D. Changes of Effective Temperature and Cold/Hot Days in Late Decades over China Based on a High Resolution Gridded Observation Dataset: Changes of Effective Temperature and Cold/Hot Days over China. *Int. J. Clim.* **2017**, *37*, 788–800. [CrossRef]
28. Bi, D.; Dix, M.; Marsland, S.; O'Farrell, S.; Sullivan, A.; Bodman, R.; Law, R.; Harman, I.; Srbinovsky, J.; Rashid, H.A.; et al. Configuration and Spin-up of ACCESS-CM2, the New Generation Australian Community Climate and Earth System Simulator Coupled Model. *J. South. Hemisph. Earth Syst. Sci.* **2020**, *70*, 225–251. [CrossRef]
29. Ziehn, T.; Chamberlain, M.A.; Law, R.M.; Lenton, A.; Bodman, R.W.; Dix, M.; Stevens, L.; Wang, Y.-P.; Srbinovsky, J. The Australian Earth System Model: ACCESS-ESM1.5. *J. South. Hemisph. Earth Syst. Sci.* **2020**, *70*, 193–214. [CrossRef]
30. Semmler, T.; Danilov, S.; Gierz, P.; Goessling, H.F.; Hegewald, J.; Hinrichs, C.; Koldunov, N.; Khosravi, N.; Mu, L.; Rackow, T.; et al. Simulations for CMIP6 with the AWI Climate Model AWI-CM-1-1. *J. Adv. Model Earth Syst.* **2020**, *12*, e2019MS002009. [CrossRef]
31. Wu, T.; Lu, Y.; Fang, Y.; Xin, X.; Li, L.; Li, W.; Jie, W.; Zhang, J.; Liu, Y.; Zhang, L.; et al. The Beijing Climate Center Climate System Model (BCC-CSM): The Main Progress from CMIP5 to CMIP6. *Geosci. Model Dev.* **2019**, *12*, 1573–1600. [CrossRef]
32. Xin, Y.; Dai, Y.; Li, J.; Rong, X.; Zhang, G. Coupling the Common Land Model to ECHAM5 Atmospheric General Circulation Model. *J. Meteorol. Res.* **2019**, *33*, 251–263. [CrossRef]
33. Swart, N.C.; Cole, J.N.S.; Kharin, V.V.; Lazare, M.; Scinocca, J.F.; Gillett, N.P.; Anstey, J.; Arora, V.; Christian, J.R.; Hanna, S.; et al. The Canadian Earth System Model Version 5 (CanESM5.0.3). *Geosci. Model Dev.* **2019**, *12*, 4823–4873. [CrossRef]
34. Sigmond, M.; Anstey, J.; Arora, V.; Digby, R.; Gillett, N.; Kharin, V.; Merryfield, W.; Reader, C.; Scinocca, J.; Swart, N.; et al. Improvements in the Canadian Earth System Model (CanESM) through Systematic Model Analysis: CanESM5.0 and CanESM5.1. *Clim. Earth Syst. Model.* **2023**, *16*, 6553–6591. [CrossRef]
35. Zhang, H.; Zhang, M.; Jin, J.; Fei, K.; Ji, D.; Wu, C.; Zhu, J.; He, J.; Chai, Z.; Xie, J.; et al. Description and Climate Simulation Performance of CAS-ESM Version 2. *J. Adv. Model Earth Syst.* **2020**, *12*, e2020MS002210. [CrossRef]

36. Gettelman, A.; Mills, M.J.; Kinnison, D.E.; Garcia, R.R.; Smith, A.K.; Marsh, D.R.; Tilmes, S.; Vitt, F.; Bardeen, C.G.; McInerny, J.; et al. The Whole Atmosphere Community Climate Model Version 6 (WACCM6). *JGR Atmos.* **2019**, *124*, 12380–12403. [CrossRef]
37. Cherchi, A.; Fogli, P.G.; Lovato, T.; Peano, D.; Iovino, D.; Gualdi, S.; Masina, S.; Scoccimarro, E.; Materia, S.; Bellucci, A.; et al. Global Mean Climate and Main Patterns of Variability in the CMCC-CM2 Coupled Model. *J. Adv. Model. Earth Syst.* **2018**, *11*, 2018MS001369. [CrossRef]
38. Lovato, T.; Peano, D.; Butenschön, M.; Materia, S.; Iovino, D.; Scoccimarro, E.; Fogli, P.G.; Cherchi, A.; Bellucci, A.; Gualdi, S.; et al. CMIP6 Simulations with the CMCC Earth System Model (CMCC-ESM2). *J. Adv. Model Earth Syst.* **2022**, *14*, e2021MS002814. [CrossRef]
39. Döscher, R.; Acosta, M.; Alessandri, A.; Anthoni, P.; Arsouze, T.; Bergman, T.; Bernardello, R.; Boussetta, S.; Caron, L.-P.; Carver, G.; et al. The EC-Earth3 Earth System Model for the Coupled Model Intercomparison Project 6. *Geosci. Model Dev.* **2022**, *15*, 2973–3020. [CrossRef]
40. Wyser, K.; Kjellström, E.; Koenigk, T.; Martins, H.; Döscher, R. Warmer Climate Projections in EC-Earth3-Veg: The Role of Changes in the Greenhouse Gas Concentrations from CMIP5 to CMIP6. *Environ. Res. Lett.* **2020**, *15*, 054020. [CrossRef]
41. He, B.; Yu, Y.; Bao, Q.; Lin, P.; Liu, H.; Li, J.; Wang, L.; Liu, Y.; Wu, G.; Chen, K.; et al. CAS FGOALS-F3-L Model Dataset Descriptions for CMIP6 DECK Experiments. *Atmos. Ocean. Sci. Lett.* **2020**, *13*, 582–588. [CrossRef]
42. Li, L.; Yu, Y.; Tang, Y.; Lin, P.; Xie, J.; Song, M.; Dong, L.; Zhou, T.; Liu, L.; Wang, L.; et al. The Flexible Global Ocean-Atmosphere-Land System Model Grid-Point Version 3 (FGOALS-g3): Description and Evaluation. *J. Adv. Model Earth Syst.* **2020**, *12*, e2019MS002012. [CrossRef]
43. Krishnan, R.; Swapna, P.; Vellore, R.; Narayanasetti, S.; Prajeesh, A.G.; Choudhury, A.D.; Singh, M.; Sabin, T.P.; Sanjay, J. The IITM Earth System Model (ESM): Development and Future Roadmap. In *Current Trends in the Representation of Physical Processes in Weather and Climate Models*; Randall, D.A., Srinivasan, J., Nanjundiah, R.S., Mukhopadhyay, P., Eds.; Springer Atmospheric Sciences; Springer: Singapore, 2019; pp. 183–195. ISBN 9789811333958.
44. Volodin, E.M.; Mortikov, E.V.; Kostrykin, S.V.; Galin, V.Y.; Lykossov, V.N.; Gritsun, A.S.; Diansky, N.A.; Gusev, A.V.; Iakovlev, N.G.; Shestakova, A.A.; et al. Simulation of the Modern Climate Using the INM-CM48 Climate Model. *Russ. J. Numer. Anal. Math. Model.* **2018**, *33*, 367–374. [CrossRef]
45. Volodin, E.M.; Mortikov, E.V.; Kostrykin, S.V.; Galin, V.Y.; Lykosov, V.N.; Gritsun, A.S.; Diansky, N.A.; Gusev, A.V.; Yakovlev, N.G. Simulation of Modern Climate with the New Version of the INM RAS Climate Model. *Izv. Atmos. Ocean. Phys.* **2017**, *53*, 142–155. [CrossRef]
46. Boucher, O.; Servonnat, J.; Albright, A.L.; Aumont, O.; Balkanski, Y.; Bastrikov, V.; Bekki, S.; Bonnet, R.; Bony, S.; Bopp, L.; et al. Presentation and Evaluation of the IPSL-CM6A-LR Climate Model. *J. Adv. Model Earth Syst.* **2020**, *12*, e2019MS002010. [CrossRef]
47. Lee, J.; Kim, J.; Sun, M.-A.; Kim, B.-H.; Moon, H.; Sung, H.M.; Kim, J.; Byun, Y.-H. Evaluation of the Korea Meteorological Administration Advanced Community Earth-System Model (K-ACE). *Asia-Pac. J. Atmos. Sci.* **2020**, *56*, 381–395. [CrossRef]
48. Tatebe, H.; Ogura, T.; Nitta, T.; Komuro, Y.; Ogochi, K.; Takemura, T.; Sudo, K.; Sekiguchi, M.; Abe, M.; Saito, F.; et al. Description and Basic Evaluation of Simulated Mean State, Internal Variability, and Climate Sensitivity in MIROC6. *Geosci. Model Dev.* **2019**, *12*, 2727–2765. [CrossRef]
49. Müller, W.A.; Jungclaus, J.H.; Mauritsen, T.; Baehr, J.; Bittner, M.; Budich, R.; Bunzel, F.; Esch, M.; Ghosh, R.; Haak, H.; et al. A Higher-resolution Version of the Max Planck Institute Earth System Model (MPI-ESM1.2-HR). *J. Adv. Model. Earth Syst.* **2018**, *10*, 1383–1413. [CrossRef]
50. Mauritsen, T.; Bader, J.; Becker, T.; Behrens, J.; Bittner, M.; Brokopf, R.; Brovkin, V.; Claussen, M.; Crueger, T.; Esch, M.; et al. Developments in the MPI-M Earth System Model Version 1.2 (MPI-ESM1.2) and Its Response to Increasing CO_2. *J. Adv. Model Earth Syst.* **2019**, *11*, 998–1038. [CrossRef]
51. Yukimoto, S.; Kawai, H.; Koshiro, T.; Oshima, N.; Yoshida, K.; Urakawa, S.; Tsujino, H.; Deushi, M.; Tanaka, T.; Hosaka, M.; et al. The Meteorological Research Institute Earth System Model Version 2.0, MRI-ESM2.0: Description and Basic Evaluation of the Physical Component. *J. Meteorol. Soc. Jpn.* **2019**, *97*, 931–965. [CrossRef]
52. Tjiputra, J.F.; Schwinger, J.; Bentsen, M.; Morée, A.L.; Gao, S.; Bethke, I.; Heinze, C.; Goris, N.; Gupta, A.; He, Y.-C.; et al. Ocean Biogeochemistry in the Norwegian Earth System Model Version 2 (NorESM2). *Geosci. Model Dev.* **2020**, *13*, 2393–2431. [CrossRef]
53. Wang, Y.; Hsu, H.; Chen, C.; Tseng, W.; Hsu, P.; Lin, C.; Chen, Y.; Jiang, L.; Lee, Y.; Liang, H.; et al. Performance of the Taiwan Earth System Model in Simulating Climate Variability Compared with Observations and CMIP6 Model Simulations. *J. Adv. Model Earth Syst.* **2021**, *13*, e2020MS002353. [CrossRef]
54. Liu, J.; Yuan, D.; Zhang, L.; Zou, X.; Song, X. Comparison of Three Statistical Downscaling Methods and Ensemble Downscaling Method Based on Bayesian Model Averaging in Upper Hanjiang River Basin, China. *Adv. Meteorol.* **2016**, *2016*, 1–12. [CrossRef]
55. Navarro-Racines, C.; Tarapues, J.; Thornton, P.; Jarvis, A.; Ramirez-Villegas, J. High-Resolution and Bias-Corrected CMIP5 Projections for Climate Change Impact Assessments. *Sci. Data* **2020**, *7*, 7. [CrossRef] [PubMed]
56. Peng, S.; Ding, Y.; Wen, Z.; Chen, Y.; Cao, Y.; Ren, J. Spatiotemporal Change and Trend Analysis of Potential Evapotranspiration over the Loess Plateau of China during 2011–2100. *Agric. For. Meteorol.* **2017**, *233*, 183–194. [CrossRef]
57. Jose, D.M.; Vincent, A.M.; Dwarakish, G.S. Improving Multiple Model Ensemble Predictions of Daily Precipitation and Temperature through Machine Learning Techniques. *Sci. Rep.* **2022**, *12*, 4678. [CrossRef] [PubMed]
58. Lei, X.; Xu, C.; Liu, F.; Song, L.; Cao, L.; Suo, N. Evaluation of CMIP6 Models and Multi-Model Ensemble for Extreme Precipitation over Arid Central Asia. *Remote Sens.* **2023**, *15*, 2376. [CrossRef]

59. Chen, W.; Jiang, Z.; Li, L. Probabilistic Projections of Climate Change over China under the SRES A1B Scenario Using 28 AOGCMs. *J. Clim.* **2011**, *24*, 4741–4756. [CrossRef]
60. Zhang, W.; Fu, J. Rainfall Erosivity Estimation Under Different Rainfall Amount. *Resour. Sci.* **2003**, *25*, 37–43.
61. Gao, G.; Zhang, J.; Liu, Y.; Ning, Z.; Fu, B.; Sivapalan, M. Spatio-Temporal Patterns of the Effects of Precipitation Variability and Land Use/Cover Changes on Long-Term Changes in Sediment Yield in the Loess Plateau, China. *Hydrol. Earth Syst. Sci.* **2017**, *21*, 4363–4378. [CrossRef]
62. Wang, S.; Fu, B.; Piao, S.; Lü, Y.; Ciais, P.; Feng, X.; Wang, Y. Reduced Sediment Transport in the Yellow River Due to Anthropogenic Changes. *Nat. Geosci.* **2016**, *9*, 38–41. [CrossRef]
63. Ullah, R.; Khan, J.; Ullah, I.; Khan, F.; Lee, Y. Investigating Drought and Flood Evolution Based on Remote Sensing Data Products over the Punjab Region in Pakistan. *Remote Sens.* **2023**, *15*, 1680. [CrossRef]
64. Yan, R.; Zhang, X.; Yan, S.; Chen, H. Estimating Soil Erosion Response to Land Use/Cover Change in a Catchment of the Loess Plateau, China. *Int. Soil Water Conserv. Res.* **2018**, *6*, 13–22. [CrossRef]
65. Qin, W.; Guo, Q.; Zuo, C.; Shan, Z.; Ma, L.; Sun, G. Spatial Distribution and Temporal Trends of Rainfall Erosivity in Mainland China for 1951–2010. *CATENA* **2016**, *147*, 177–186. [CrossRef]
66. Gao, G.; Han, Z.; Yin, S.; Huang, D.; Wang, W. Characteristics of Rainfall Erosivity During 1961 2017 and lts Change Projections in Future in the Yellow River Basin. *J. Basic Sci. Eng.* **2021**, *29*, 575–590. [CrossRef]
67. Li, Z.; Liu, T.; Huang, Y.; Peng, J.; Ling, Y. Evaluation of the CMIP6 Precipitation Simulations Over Global Land. *Earth's Future* **2022**, *10*, e2021EF002500. [CrossRef]
68. Kou, P.; Xu, Q.; Jin, Z.; Yunus, A.P.; Luo, X.; Liu, M. Complex Anthropogenic Interaction on Vegetation Greening in the Chinese Loess Plateau. *Sci. Total Environ.* **2021**, *778*, 146065. [CrossRef]